Student thesis series INES nr 571

Fragmentation in graupel-snow collisions

Martanda Gautam

2022
Department of
Physical Geography and Ecosystem Science
Lund University
Sölvegatan 12
S-223 62 Lund
Sweden

Martanda Gautam (2022).
Fragmentation in graupel-snow collisions
Master's degree thesis, 30 credits in *Atmospheric Sciences and Biochemical Cycles*
Department of Physical Geography and Ecosystem Science, Lund University

Level: Master of Science (MSc)

Course duration: *January* 2022 until *June* 2022

Disclaimer

Fragmentation in graupel-snow collisions

Martanda Gautam

Master thesis, 30 credits, in Atmospheric Sciences and Biochemical Cycles

Supervisor 1:
Vaughan Phillips,
Department of Physical Geography and Ecosystem Science
Lund University

Supervisor 2:
Marcin Jackowicz – Korczynski,
Department of Physical Geography and Ecosystem Science
Lund University

Exam Committee:

Vilhelm Malmborg,
Department of Design Sciences, LTH
Lund University
Sachin Patade,
Department of Physical Geography and Ecosystem Science
Lund University

Acknowledgments

At the very outset, I would like to thank my supervisors Dr. Vaughan T.J. Phillips, Dr. Marcin Jackowicz-Korczynski and the course coordinator Dr. Martin Berggren for their insightful knowledge, academic support, and motivation. I would also like to thank the Department of Physical Geography and Ecosystem Sciences, along with CGB Kansli for providing me with the necessary administrative help and support during the project period. I am very grateful to the Staff at ICOS Svartberget Research Station., esp. Dr. Paul Smith, Dr. Johan Westin and Dr. Guiseppe De Simon for their help in making my field trip feasible, providing me with meteorological station data, and the entire station staff for lending a supporting hand during the data collection period. I am also thankful to Dr. Meelis Mölder and Dr. Patrik Vestin for sharing their intellectual acuity during the study period.

I am hugely thankful to Dr. Sachin Patade, for his help in getting me accustomed to the fragmentation scheme within the Aerosol-Cloud model and perceptive insights into the theoretical aspects of it, and to Mr. Deepak Waman for his immense help with the estimation of rime fraction for individual particle sizes and related theoretical formulations. I am also grateful to Mr. Per-Erik Fahlen for his help during the construction of the chamber. I would like to express my gratitude to Ms. Priyanka Baishya for her insights and constant encouragement in a time of need, and to Mr. Sandro Brustharnisch, Mr Anirudh H. Kashyap, and Mr Peter Kornacher for their support in providing me with additional camera and other equipment during the field work.

Abstract

Aircraft observations of precipitating clouds with cloud top temperatures higher than -38°C, have revealed that Secondary Ice Production (SIP) is responsible for the presence of majority of ice particles. One such SIP mechanism is fragmentation via collisions between ice particles. The central theme of this study is to understand the dependencies of this SIP mechanism and improve its existing numerical and theoretical predictions, through field-based observations.

This study is motivated by the only field experiment to observe this type of mechanism, by Vardiman in 1978, who built a probe to sample falling ice precipitation outdoors. We modify aspects of that study by building our own portable chamber with knowledge from more recent publications and advances in technology. Fragmentation of individual snowflakes falling into it was recorded with high-speed video cameras. An array of 126 ice spheres were fixed to the base of the chamber and each was assumed to be representative of graupel. With this chamber, fragments from each collision between a falling snowflake and an ice sphere could be counted and sized from inspection of video recordings, after sampling outdoors.

There was a field trip to sample naturally falling snow particles in the Svartberget forest in Vindeln, in the north of Sweden, about 650 km south of the Arctic Circle on 24 February 2022, around midnight UTC. It was a snowfall lasting about 4 hours from an orographic stratiform cloud (with precipitation rate of about 7 mm/hr) with a mixed-phase cloud top of about -20°C and a cloud base of -2.6°C about 100m above the ground (elevation 270 metres MSL). Simultaneously the mass-size relationship parameters for the falling snow particles were measured, which enabled the mass of each snow particle in the chamber to be estimated from its size before collision.

The results for the average size distribution of fragments, the coincident mass-size parameters, fall speed–size relation, and dependencies on Collision Kinetic Energy (CKE) correspond well with previously reported studies for dendritic snow. From the observed number of fragments, we refitted the theoretical formulation for this type of fragmentation in graupel snow collisions. For this formulation, a new form of the dependence of rime fraction on size is inferred from the coincident measurements of axial ratio. This refitting yielded an improved value of the asperity-fragility coefficient, C, of about 3.86×10^4 J^{-1} for dendritic snow colliding with graupel. Our field observations suggest that fragmentation in graupel-snow collisions is even more profound (about 3 times higher) than the previous estimations from the original version of the formulation. And a new revised version of the formulation is proposed for use in atmospheric cloud models.

Keywords: Ecosystem Analysis, Clouds, Snow, Graupel, SIP, Fragmentation, CKE, Rime Fraction

List of abbreviation

IN	Ice Nucleus
INPt	Ice Nucleating Particle
SIP	Secondary Ice particle
CKE	Collision Kinetic energy
C	Asperity-fragility coefficient
Chi (χ)	Rimed mass fraction for an ice particle
Psi (ψ)	Correction factor for fragmentation scheme

List of Tables

List of Figures

Table of contents **Page No**

1. Introduction

Cloud systems form an essential part of ecosystems sustaining life on Earth. Clouds act to shield the surface from incoming shortwave radiation, and trap outgoing longwave radiation. They also provide life at the Earth's surface with water in the form of precipitation (rain and snow). Precipitation in the form of rain occurs when water vapour condenses onto droplets which further undergoes coalescence growth until the raindrops are heavy enough to descend from the clouds. If rain forms at subzero levels, then supercooled rain can freeze to form graupel/hail, which is dense ice precipitation that grows by riming.

The understanding of ice crystal formation in clouds is a complex phenomenon. The generation of ice crystals from an ice nucleus (IN) in colder clouds has been a much-researched entity in the research community. Experimental observations from airborne, drone flights and other remotely sensed datasets reported to have found higher concentrations of ice nucleating particles (INP) than expected from primary ice nucleation processes (Kanji et al, 2017). This led to the formulation of concepts of SIP and different mechanisms or pathways have been studied which could potentially account for the higher concentration of observed IN (Yau and Rogers, 1996, Ch 9). Consequently, SIP within clouds has been believed to be the major source of generation of ice crystals leading to subsequent snowflakes, graupel, hail and so on (Pruppacher and Klett 1997, their Ch 14-16, Field et al, 2016).

One such pathway for SIP is via fragmentation due to collisions among ice particles, and an experimental study about this mechanism is the central theme of this report. In a preliminary study by Phillips et al. (2017a), a theoretical formulation of fragmentation in ice-ice collisions was created for all permutations of pairs of colliding microphysical species, as explained in Sec. 3.6. When this scheme was implemented in two cloud models, graupel-snow collisions were found to be the most profound in total numbers of fragments emitted throughout a simulated multi cell convective storm. (Phillips et al, 2017b).

Eventually, the goal of the present study is to observe experimentally the suitability of the fragmentation mechanism in graupel-snow collisions. And possibly represent the findings with an updated parameterization of this theoretical formulation of fragmentation from Phillips et al. (2017a). The need to improve it is apparent from the under-prediction of ice crystal concentrations when implementing it in simulations of Arctic supercooled clouds (Sotiropoulou et al, 2021). The motivation is to provide the scientific community with a modelling tool to allow better understanding of the role of this prevalent mechanism of SIP, which naturally occurs in clouds (Phillips et al, 2017b; Huang et al, 2021; Sotiropoulou et al, 2021; Zhao et al, 2021).

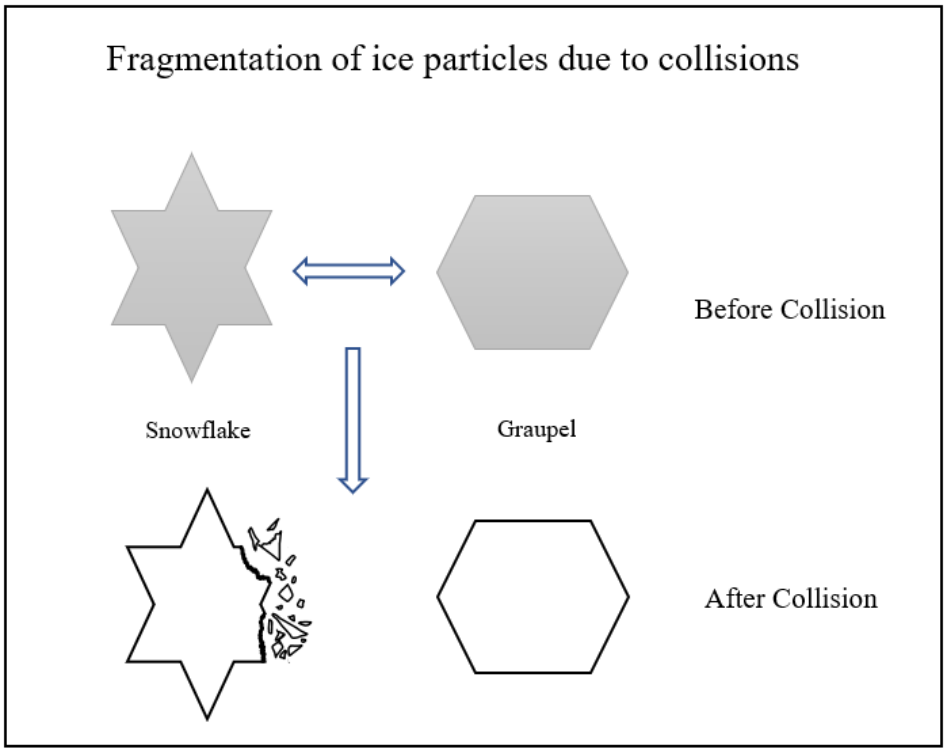

Fig. 1 A visualization of secondary ice production via fragmentation process, studied in this report.

Until now only two major studies have reported experimentally determined rates of ice fragmentation in collisions: 1) Vardiman (1978 a, b) observed fragmentation of naturally falling ice particles outdoors on a mountainside, partly with a chamber containing a fixed metal mesh structure; 2) Takahashi et al, (1995) observed in the lab collisions between a pair of giant ice spheres (replicating hail particles) with rotating metal rods at different fall speeds and temperatures.

In the present study, the experimental setup was broadly similar to that constructed by Vardiman (1978b), modifying certain aspects in the design. It involves a chamber into which naturally falling snow particles underwent collisions with a metal mesh structure. The number of fragments produced from the collisions were collected on a tray with supercooled sugar solution, at the bottom of the chamber. Images of the fragments collected on the tray were used for counting and size measurements (Vardiman 1978b). In light of more recent studies (e.g., Dong et al, 1994) and advances in technology we modified Vardiman's setup in the following respects:

(1) Sampling during ice-supersaturated cloudy conditions (almost foggy) to avoid any sublimational weakening of the ice precipitation falling below cloud.

(2) Video camera with high frame rate.

(3) An array of ice spheres replicating graupel particles instead of a metal mesh structure.

(4) LED lights with low heat emission.

(5) Use of coincident radar and satellite observations with Re-Analysis datasets from ECMWF (European Centre for Medium-Range Weather Forecasts) to constrain cloud characteristics at the sampling location.

Additionally, mass-size relation parameters (α, related to density and b, dimensionless parameter) of the falling snow particles were measured at the same location to infer the masses of individual snow particles sampled in the chamber. CKEs were calculated from the measured fall speeds and inferred masses. The mass-size relation for a given type of ice particles is (Yau and Rogers, 1996, their Ch 9):

$$m = \alpha D^b \qquad (1)$$

Here, m is the mass (in grams), D is the diameter of a snowflake's major dimension (in cm), α is a parameter (in g/cm) that relates to the density of the snowflake, and b is the fractional diameter of the particle, a dimensionless quantity.

Essential requirements for the fragmentation scheme designed by Phillips et al. (2017a) involved data on size and mass of the ice particles, their CKE, temperature of most of the growth of the snow (dendritic vs non-dendritic), and rime fraction of the ice particles (χ) . In the fragmentation scheme an asperity-fragility coefficient, C, multiplies the CKE inside the exponential function for the number of fragments per collision (Sec. 3.6). The scheme assumes that this number approaches an upper limit asymptotically in an exponential manner and the upper limit depends on the ice surface area. In this formulation (Phillips et al, 2017a), observational data from the Vardiman (1978b) field experiment was used and rescaled (using a correction factor ψ) to agree with the Takahashi lab experiment (Takahashi et al, 1995).

Conceptual visualization of the naturally occurring fragmentation process is shown in Figure 1. The collision between a snowflake and a graupel particle would result in splitting of the less dense snowflake, into several fragments. In this study, frozen drops that are ice spheres would mimic a graupel particle (Figure 1) and fragmentation of incident snowflakes is measured. The central aim of this study will be to improve on the formulation of C, and relating this fragmentation via collisions to CKE and particle sizes, with the help of experimental observations. And this could further help in modelling of this SIP in natural clouds.

2. Aim:

The aim of this study is to characterize a fragmentation mechanism of SIP, namely fragmentation in graupel-snow collisions and advance understanding of its dependencies. A related aim is to improve existing numerical and theoretical predictions of SIP via fragmentation. Alongside the following research topics and questions will be addressed in this report:

a. Is it possible to experimentally observe the rate of Secondary Ice Production (SIP) of crystals due to graupel-snow collisions and relate it to theoretical formulations already published?

b. How to experimentally derive the mass-size relationship parameters (α and b) with a simple setup? Subsequently, obtain CKE for each collision event and optimise the asperity-fragility coefficient (C) for fragmentation due to ice-ice collision, which can help improve the existing cloud models.

c. Does the fragmentation process conform with theoretically expected dependencies on size and CKE?

3. Background:

3.1 Clouds : an overview

Clouds are formed due to vertical motions of air molecules, convection, and mixing processes. Cloud microphysical processes are forced by in-cloud dynamics in nature, which in turn are influenced by vertical profiles of heat and moisture in the environment (Yau and Rogers, 1996, their Ch 5). Clouds are also influenced by other physical phenomena such as latent heat release and the distribution of atmospheric water vapour. Thermodynamic responses of the environment to shortwave and longwave radiation can affect all of these factors.

Clouds may be viewed as being in a continuous transition cycle between two major events, one where droplets are continuously created due to condensation in ascent and the other where they are simultaneously lost due to evaporation and precipitation. Clouds are broadly classified into three major types based on their appearance from the ground, as proposed by Luke Howard in 1803. They are

- convective (cumulus): vertically developing clouds.
- stratiform (stratus): flat and layered clouds.
- cirriform (cirrus): hair/feather-like clouds.

Besides these, clouds are also further categorised by the combination of these three types and by their other characteristics (e.g., rain bearing: nimbus) and altitude in the troposphere.

3.2 Warm Clouds

Regarding warm clouds, the formation of cloud droplets is governed by phase transitions of water. The initial process is the formation of Cloud Condensation Nuclei (CCN) (Yau and Rogers, 1996, their Ch 6). In the atmosphere, there are small hydrophilic (affinity towards water) particles of the size of a micrometre or even smaller (aerosols from dust, smoke, vehicle exhaust, etc.), which become the cores for condensation and subsequently lead to formation of water droplets. Aerosols are very fine, tiny (with diameters around or less than 1 μm) solid or liquid particles which remain suspended in the air. The resulting droplets from condensation (diffusion of water vapour into the surface of the droplet) vary in size and concentration depending mostly on vapour pressure, temperature, and motions of air molecules (Yau and Rogers, 1996, their Ch 7).

3.3 Ice formation

Ice particles are also initiated from phase transitions from either water or vapour. Ice formation is considered to be a major phenomenon for the occurrence of precipitation (Lau and Wu, 2003). In cold clouds, ice crystals are formed in cloudy air supersaturated with respect to ice (relative humidity with respect to ice higher than 100%) when it reaches sub

zero temperatures. Crystals grow mainly via the diffusion of vapour from the ambient cloudy air. Whereas CCN are the basis of cloud droplets, ice crystals can be initiated by a variety of possible mechanisms, including the activity of ice nucleus (IN) aerosol particles, and via SIP mechanisms involving fragmentation of pre-existing ice (Yau and Rogers, 1996, their Ch 9).

Figure 2 shows the different mechanisms for the initiation of ice nucleation. There is homogenous freezing of any supercooled water/cloud droplets at sub zero temperatures (less than -38°C), which in the upper troposphere mostly forms cirrus clouds (Yau and Rogers, 1996 their Ch 8; Lau and Wu, 2003). IN may also initiate ice formation at temperatures between 0 and -38°C in mixed phase clouds in the lower and middle tropospheric region (Yau and Rogers, 1996 their Ch 9; Pruppacher and Klett 1997, their Ch 13; Murray et al, 2012). Initiation of ice from IN aerosols is in the category of heterogeneous nucleation, since a foreign particle initiates the nucleation process (Yau and Rogers, 1996, their Ch 9; Pruppacher and Klett 1997, their Ch 13). Such nucleation can occur at lower supersaturations and higher temperatures as compared to homogeneous nucleation (Yau and Rogers, 1996 their Ch 9; Pruppacher and Klett 1997, their Ch 13; Murray et al, 2012).

In the deposition nucleation mode, direct deposition of water vapour onto IN material in an ice-supersaturated environment is seen. For the case of the condensation freezing mechanism, aerosols after acting as CCN, initiate freezing of supercooled cloud droplets (Yau and Rogers, 1996 their Ch 9; Murray et al, 2012). Also contact between primitive ice structure (also called ice embryos) and supercooled droplets also lead to formation of IN (also shown in Figure 2) (Yau and Rogers, 1996 their Ch 9; Pruppacher and Klett 1997, their Ch 13; Murray et al, 2012).

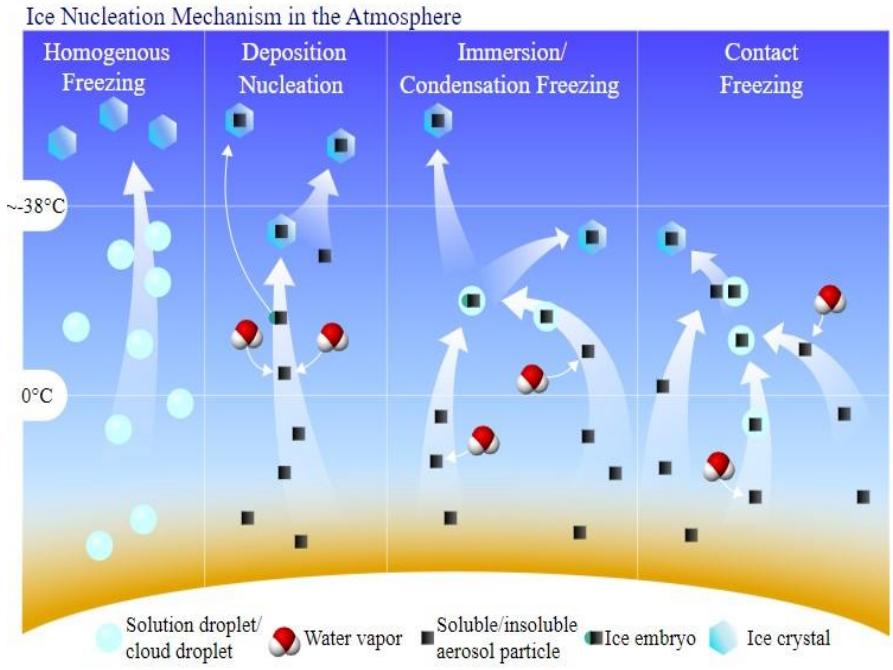

Figure 2. Ice nucleation mechanisms. [Adopted from https://commons.wikimedia.org/wiki/File:Ice_Nucleation_Mechanisms.svg with license from https://creativecommons.org/licenses/by-nc/4.0/legalcode]

For SIP, there are many possibilities involving fragmentation of precipitation. There can be breakup in collisions between ice crystals, shattering of freezing drops, the rime-splintering process, fragmentation caused by thermal shock, or due to sublimation of ice (Pruppacher and Klett 1997, their Ch 14-16; Field et al, 2016). These are further explained in the Section 3.5

3.4 Types of Ice Crystals

Size and shapes of naturally occurring snow crystals are highly dependent on temperature and on the extent of supersaturation with respect to ice, as has been verified by various experiments. Figure 3 shows the conditions for ambient temperature and humidity for growth of natural snow crystals (Pruppacher and Klett 1997, their Ch 2; Magono and Lee, 1966; Bailey and Hallett, 2004). Commonly found crystals include planar, dendritic, rimed crystal, planar crystal with broad branches, graupel, needle shaped, hollow and solid columns and bullet shaped. Experimental studies have found further variation in the commonly observed shapes, and they are dependent on the thermodynamic conditions in clouds.
Furthermore, the growth characteristics (shape and structure) can change in case there is a change of local ambient temperature and humidity. For instance, when a snow crystal growing at a certain habit (temperature and humidity) is falls into new ambient conditions, then effects from the newer conditions get superimposed on the growth of the original crystal structure (Pruppacher and Klett 1997, their Ch 2). One could observe an originally column shaped snow crystal developing planar structures with change of growth habit. In the scope of the present study, dendritic and graupel regimes have been primarily focussed.

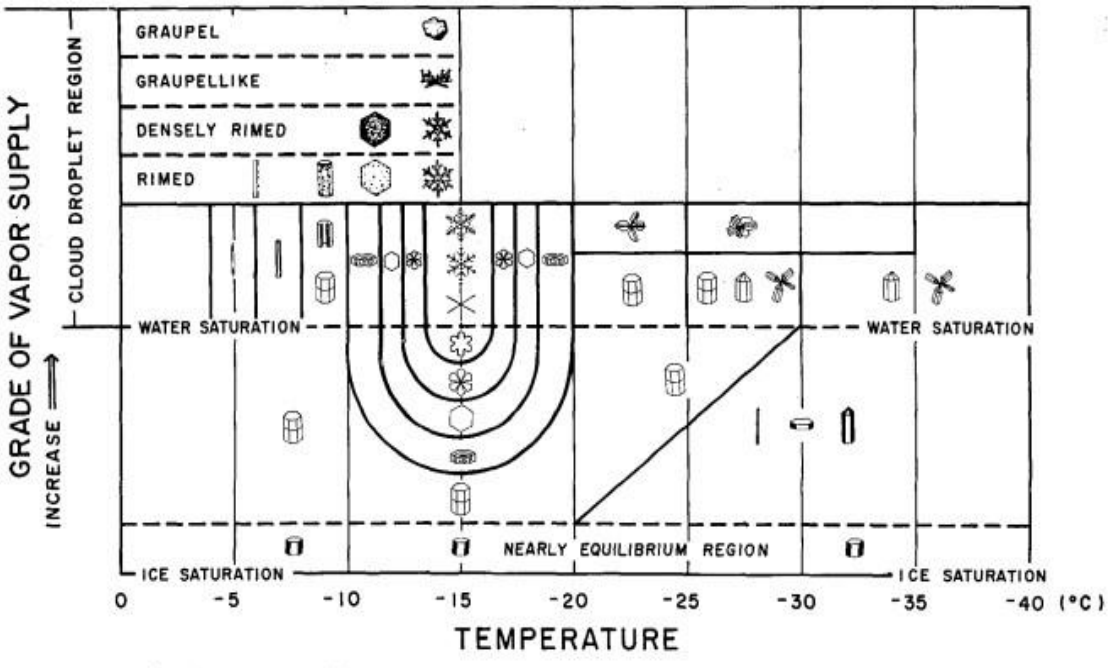

Figure 3. Magono-Lee diagram showing temperature and humidity variation for growth of different types of natural ice crystals. [Adopted from Magono and Lee. 1966, with permission under Japanese Copyright Act, Article 32(1)
https://www.bunka.go.jp/seisaku/chosakuken/seidokaisetsu/gaiyo/chosakubutsu_jiyu.html]

3.5 Secondary Ice Production

As mentioned previously, concentrations of ice particles in clouds are observed to orders of magnitude higher than coincident concentrations of IN in the local environment, which implies generation of ice particles somehow via secondary means (Field et al, 2016; Pruppacher and Klett 1997, their Ch 14-16; Yau and Rogers 1996, their Ch 9). Figure 3 shows various known SIP mechanisms.

The rime splintering mechanism, also known as Hallet-Mossop process (Hallett and Massop 1974; Field et al, 2016) is one of the most studied SIP pathways (Figure 4). When large ice particles (e.g., graupel-like) collect supercooled liquid droplets along their paths (also called riming) inside the cloud system, they eject ice splinters which will further grow to become needles, columns or planars (Hallett and Massop 1974). Experimental verification indicates a set of favourable conditions for rime splintering: a) temperature range of – 3°C to -8 °C for this process to be active, b) supercooled droplets with size greater than 23µm and c) fall speed in the range 0.2 to 5 m/s (Hallett and Massop 1974, Field et al, 2016). Larger ice crystals could give rise to numerous splinters, leading to higher concentration of ice particles inside the cloud system (Field et al, 2016; Zhao and Liu 2021).

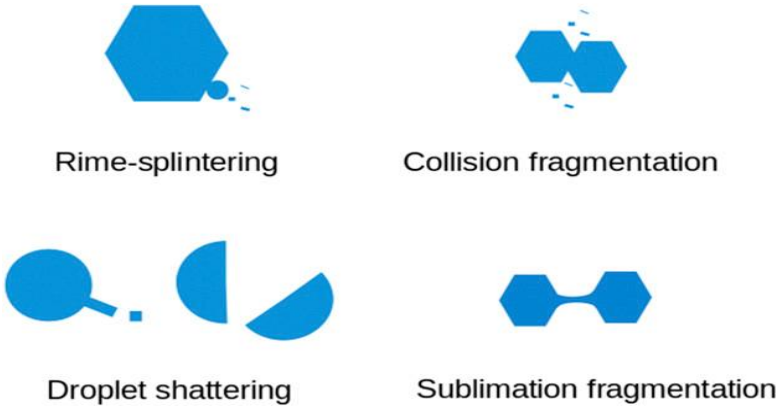

Figure 4. Different SIP mechanisms. [Adopted from Field et al, 2016, with permission from Meteorological Monographs]

Another accepted SIP pathway is via fragmentation in ice-ice collisions (see Figure 4), (Yau and Rogers, 1996, their Ch 9; Pruppacher and Klett 1997, their Ch 14-16; Field et al, 2016). Ice crystals being found in different shapes and sizes and moving with different velocities, would give rise to numerous fragments upon collision between them. Vardiman, (1978 a, b) and Takahashi et al, (1995) performed experimental verification of this process. Vardiman, (1978b) studied the fragmentation process by allowing snow particles to collide with a metal mesh structure and record the process of fragmentation. By contrast, Takahashi et al, (1995), observed the collision of larger graupel particles. Moreover, James et al, 2021 measured the production of secondary ice particles via collision of frozen water drops with more massive ice particles.

Yano and Phillips (2011) theoretically elucidated the role of fragmentation via ice-ice collisions and emphasized that it could potentially be more prolific as a SIP process than the previously considered Hallett-Mossop process, which requires a certain temperature range for it to be active. Under favourable conditions, such as the existence of graupel particles in the millimetre range, a higher concentration of ice crystals involving positive feedback (chain reaction) with ice multiplication (growth of fragments to become fragmenting precipitation) could lead to production of very high concentrations of ice crystals (Yano and Phillips, 2011).

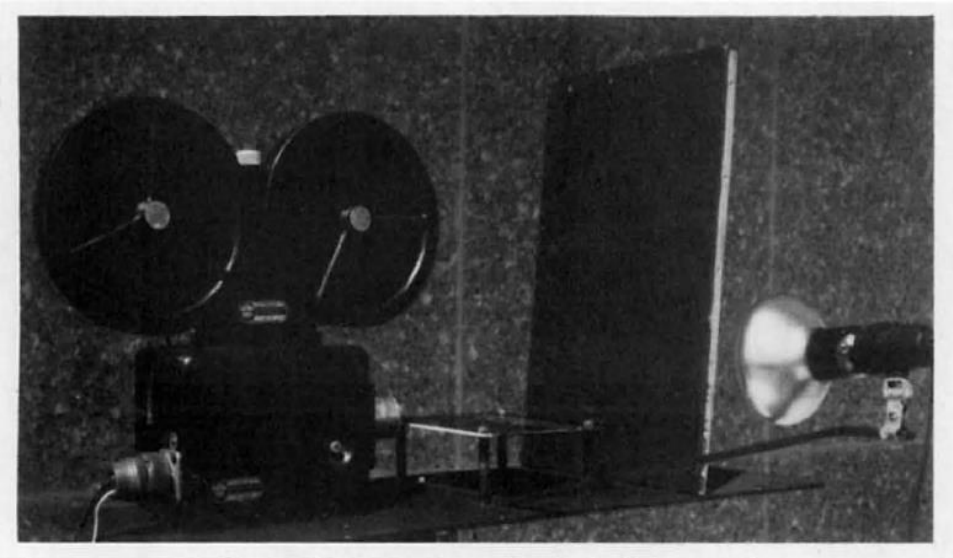

Figure 5. Photographic instrument used in the Larry Vardiman's (1978b) fixed plate experiment. The high-speed camera (DMB 4, 16 mm) apparatus located at left of the image, followed by fixed metal plate. [adapted from Vardiman, (1978b), with permission from Journal of the Atmospheric Sciences].

SIP can also be achieved via thermal shock due to a thermal imbalance created when a supercooled droplet undergoes riming along the surface of an ice crystal creating a temperature gradient and resulting in fracture of the ice crystal and thus generating more ice crystals (Field et al, 2016). Sublimation refers to the phase change directly from ice into vapor. During sublimation (Figure 4) of large riming particles, several secondary ice particles could also be generated as well (Bacon et al, 1998; Field et al, 2016).

3.6 Original Version of the Theoretical Formulation of Fragmentation from Literature

A formulation was proposed by Phillips et al. (2017a), for the number of fragments for any collision of a pair of ice particles in any permutation of microphysical species (e.g., Graupel-graupel, graupel-snow, snow-crystal, graupel-crystal). The formulation was theoretically based on principles from classical mechanics: conservation of energy and statistical variations of ice asperities on the microscopic scale. Some essential features are as follows.

Any object or particle in motion has kinetic energy. During a collision there is a transfer of energy as well as momentum. If the collisions are perfectly elastic in nature, then both kinetic

energy and momentum are conserved, being unchanged after a collision. However, in the case of inelastic collisions, the total kinetic energy of the system is not the same after a collision. For two particles having masses m_1 and m_2, with initial velocities v_1 and v_2, their collision kinetic energy (CKE) is given by:

$$CKE = \frac{1}{2}\frac{(m_1 \times m_2)}{(m_1 + m_2)}(\overrightarrow{v_1} - \overrightarrow{v_2})^2 \quad (2)$$

In this study, the graupel particle is stationary, hence the CKE, for a single particle (with mass m and velocity v) in motion is given by $\acute{CKE}$:

$$\acute{CKE} = \frac{1}{2}m\vec{v}^2 \quad (3)$$

The fragmentation scheme from Phillips et al. (2017a) for the number of fragments in any ice-ice collision is:

$$N = \alpha A(\mathbf{M}) \left(1 - \exp\left\{-\left[\frac{CK_0}{\alpha A(\mathbf{M})}\right]^{\gamma}\right\}\right) \quad (4)$$

Here, N is the number of predicted fragments; $A(\mathbf{M})$ is the number density of breakable vapour grown branches per unit area of the surface of the more fragile particle. **M** refers to the type of colliding particles. The parameter α is the spherical equivalent area (in m^2) of a snow particle. C (J^{-1}) is the asperity-fragility coefficient which depends on the microphysical species and morphology of the colliding particles. For dendritic snow particles $C = 3.09 \times 10^6\, \psi$ J^{-1}, where $\psi = 3.5 \times 10^{-3}$ is the correction factor. The correction factor (ψ) was intended to compensate for the sublimational weakening of snow particles in the field experiment by Vardiman (1978 a, b) but include other differences between the Vardiman and Takahashi experiments too. The parameter K_0 is the initial CKE before collision in Joules (J). Parameter γ is a dimensionless exponent affecting the dependency of number of fragments (N) on CKE and was inferred from lab observations by Takahashi et al. (1995). For dendritic particles, it takes a value of γ = 0.5-0.25χ . And χ is the mass fraction of an ice crystal or snow particle that is rime (cloud droplets frozen on impact during accretion by the ice) and is less than 0.5 for snow particles.

This scheme (Eq(4)) is based on the conservation of kinetic energy which predicts the number of fragments produced during a collision event for a specific ice particle size and type (Phillips et. al. 2017a). Along with dimensions, spherical equivalent volume, initial collision kinetic energy, there are other parameters which are essential in the realization of the entire scheme. Temperature plays a prominent role in these fragmentation regimes: for each type of crystal in their specific growth habit, specific temperature intervals are set (Phillips et al, 2017a). For snow particles that have mostly grown in the dendritic regime, we set T to a value between -12°C and -17°C, in accordance with observed growth regimes (Magono and Lee, 1966).

4. Methodology

4.1 Study Area

Data collection was done in a naturally snowing environment during nearly foggy conditions (humidity near water saturation) at the ICOS (Integrated Carbon Observation System) Svartberget Research Station (64°15′N, 19°46′E) for a period of 3 weeks, from 17th February 2022 to 9th of March. The research station is located at an elevation of 270 metres above sea level, about 60 km west of Umeå, and is in the midst of Svartberget experimental forest (1076 ha in area). Svartberget is also a part of the Swedish Infrastructure for Ecosystem Science (SITES).

Figure 6. Sampling location. Google earth imagery of the location where the data collection was done.

4.2 Chamber Design

To record the fragmentation process, a transparent rectangular chamber ($40 \times 30 \times 30$cm) was constructed using Plexiglass material (4 mm thickness). Its design was inspired by the one designed by Vardiman (1978b). A 2D schematic of the experimental setup is shown in Figure 7. Images of the constructed chamber, used in the field, are shown in Figure 8.

The top of the chamber had a small lid (denoted by 'T', Figure 7) with dimensions of 8×8 cm. This opening was intended to allow one or two snow particles to fall inside the chamber in any sampling event. During instances of heavier snowfall, the size of the opening was reduced to a circle with 2.5 cm in diameter. A data logger (denoted by 'D', Figure7) was placed for recording the temperature and relative humidity inside the chamber. The chamber was illuminated with different LED lights (denoted by 'L1','L2') with various intensities (1200, 600 and 300 lumens). The positioning of the light sources as well their intensities were varied according to the availability of natural light. For recordings done during the daytime (data not presented in this report), light sources with combined intensity of 300 lumens were used, whereas, for night-time recordings, light sources with 600 lumens and 1200 lumens were used. The positioning of the light sources was such that the main beam was focused on the target area (denoted by 'M').

The target area was comprised of an array of 126 frozen drops arranged on a Cartesian grid near the base of the chamber, such that each snow particle entering the chamber would be likely to collide with one of them. The frozen drops were supported on a vertical grid-like structure made with aluminium wires (2 mm diameter) and each grid placed 40 mm apart from each other. From each wire on the vertical grid, there were metal spikes (1.5 mm diameter) protruding out at an angle of 45°from the horizontal plane. Consecutive spikes were placed 20 mm apart from each other. Ice spheres (sizes varied from 3 mm – 8 mm in diameter) were created at the ends of these spikes by freezing drops of supercooled water in an open top freezer at sub zero temperatures. Smaller sizes (lower than 3 mm) of graupel particles do exist, however, a specific size range for the ice spheres (3 mm – 8 mm) were chosen. This was done to maximise the probability of fragmentation, by increasing the surface area, for the incident snowflakes to collide with. The average spacing of neighbouring ice spheres was 15-20 mm. The ice spheres were prepared 1 day prior to a predicted snowfall forecast.

At the base of the chamber, below the array of frozen drops, a tray of supercooled sugar solution was placed to collect the fragments of snow after collision had taken place. This provided extra guidance when identifying the collision in the video film from cameras afterwards. Two cameras (denoted by 'C1' and 'C2') were used during the sampling process, one focused on the target array (with ice spheres) with a slanted view, and another one focussed on the tray with supercooled sugar solution (denoted by 'S') with a vertical view, to record the collected fragments at the end of collisions. The tray was marked with grid lines at a distance of 2 cm between each subsequent line. Both recordings were carried out at 120 frames per second. The minimum resolution of both the cameras were 0.2 mm. Fragment sizes lower than 0.2 mm have been estimated by measuring the fraction of pixel illumination area relative to the total area of the smallest pixel, from the images extracted from video recordings. Error in measurement arising from this approach (for fragment size smaller than 0.2 mm) has been roughly estimated and addressed in Sec. 6.2.

In summary, naturally falling snow particles were allowed to collide with ice spheres replicating graupel particles, and fragmentation events were recorded.

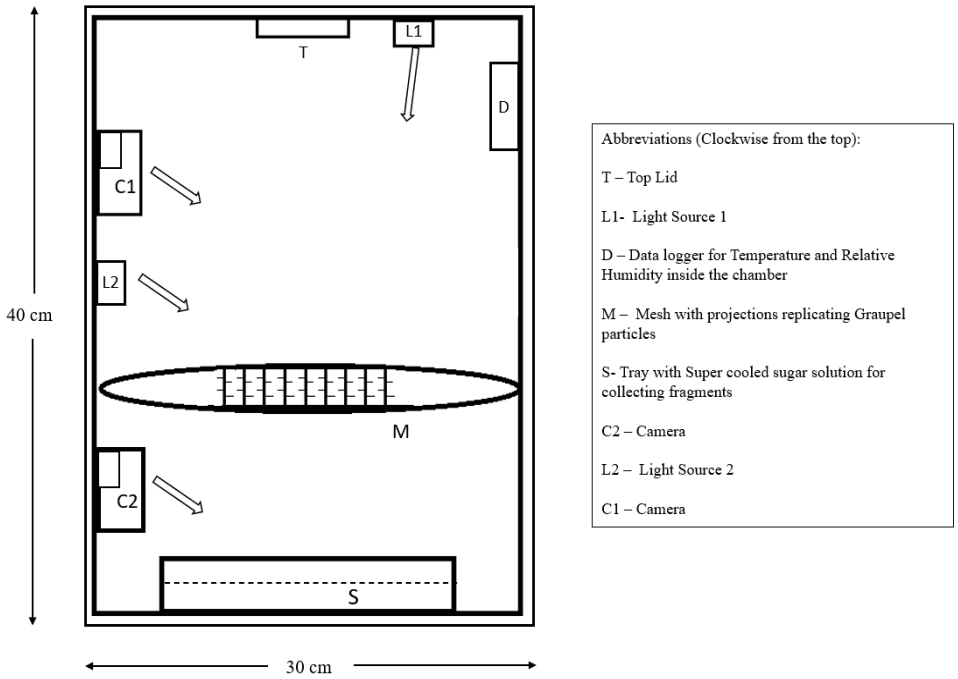

Figure 7: A 2D visualization of the acrylic chamber to be constructed for the experiment.

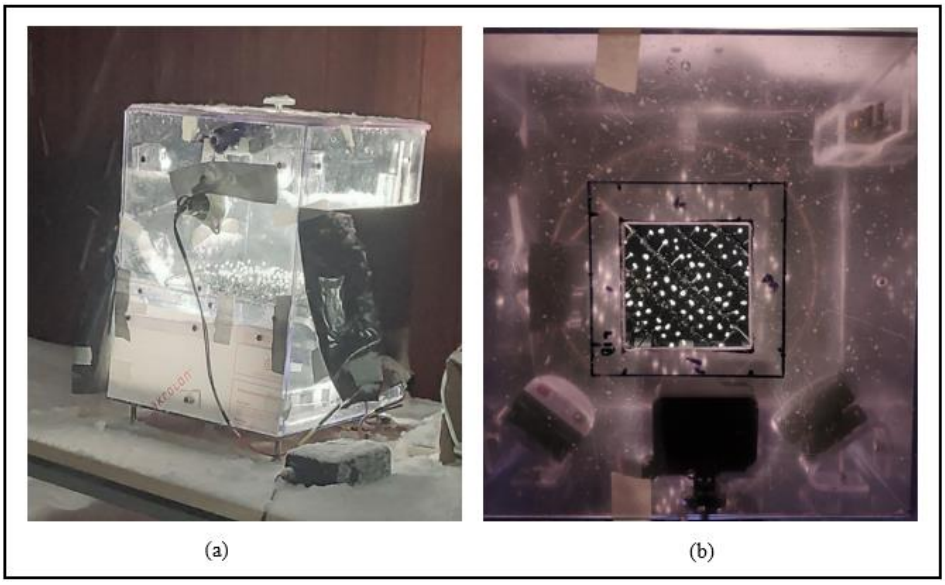

Figure 8. Images of the actual Chamber in the field. (a) during a sampling event (b) top view of the chamber

4.2.1 Equipment Specifications

- Camera – Go Pro Hero 5 and Go pro Hero 6
- Data logger – TH-680L, by Exotek Instruments.

4.2.2 Supercooled sugar solution

Addition of solute (sugar- sucrose) to a solvent (water) affects the colligative properties of the solvent such as elevating its boiling point, lowering of freezing point and rise in osmotic pressure of the solvent (Atkins and de Paula 2006). The empirical equation for depression of freezing point used is this study is:

$$\Delta T_f = K_f b \qquad (4)$$

Here, ΔT_f is the change in temperature (Kelvin), K_f is the cryoscopic constant (K Kg/mol) and b is the molality of the solution (mol/kg).

The prepared sugar solution was seen to have a freezing point of -13°C. The supercooled solution preserved the fallen fragments for long enough to be recorded and protected them from sublimation.

4.3 Sampling

During the above-mentioned period of 3 weeks, five major snowfall episodes were encountered, wherein data collection was done. The temperature and humidity parameters recorded during those snowfall events are shown in Table 1.

Table 1: Showing the temperatures and relative humidity during the 5 snowfall episodes. T_{air} and RH_{air} is obtained from CR1000 (Campbell Scientific) logger connected at a height of 1 metre on the main flux tower at Svartberget Research Station. The day selected for analysis in this present study is denoted in bold.

Date and Time (Central European Time)	T_{air} (°C)	RH_{air} (%)	Snowfall Type
18-2-2022 (20:00)	-7.40	81.75	Light, dry powder
24-2-2022 (01:00)	**-2.61**	**95.20**	**Moderate, aggregates**
1-3-2022 (11:00)	0.37	85.09	Light, dry powder
7-3-2022 (16:00)	2.76	94.41	Light, aggregates
9-3-2022 (23:30)	-2.73	94.99	Very Light, dry powder

However, only one of these five episodes was analysed here in this present study, because it had a more intense snowfall rate with ice particle aggregates (snowflakes). This episode happened on 24th February 2022 and captured the fragmentation process of graupel snow collisions most effectively and clearly. Another reason for analysing data for a single day is

the sheer volume of data (54,592 images) and limited duration of the present project. Images of snowflake particles during the selected episode is shown in Figure 9.

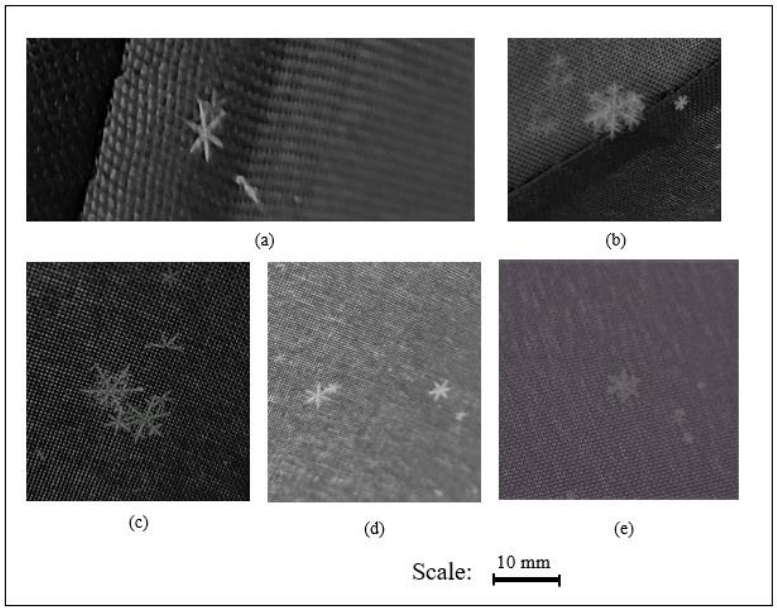

Figure 9. Images of the incident snowflakes during the 24th of February sampling event.

4.3.1 Chamber Stabilization:

A stabilization period was required for the chamber, with the lids removed and vents open, to adjust to the ambient conditions with respect to air temperature and humidity. The stabilization period however was not fixed during all the sampling events; it varied from 3 to 5 hrs, mostly depending on the air temperature. Colder air temperatures and highly humid conditions would lead to faster stabilization of the chamber. When not in use, the chamber was kept inside a cold room at a temperature of 2°C, so as to minimise the stabilization period.

Precipitation and wind radar updates from SMHI (Swedish Meteorological and Hydrological Institute) were checked prior to, and during, each snowfall episode. Accordingly, chamber was prepared outdoors for stabilization when anticipating it.

4.3.2 Sampling: Fragmentation process

Sampling for recording the fragmentation process via collisions, was done by opening the lid of the chamber for a period of 2 minutes followed by cleaning of the target (ice spheres) with a paintbrush. Snow particles and fragments from the sugar solution tray were removed with a teaspoon. In case of a light snowfall episode, the top lid would be kept open for a longer period (5-10 minutes), followed by the cleaning steps. Multiple samplings were carried out over the duration of a snowfall episode. During windy conditions, improvised wind shelters were built using snow-sticks and plastic sheets.

4.3.3 Sampling: Mass size relation

To estimate the mass size relationship of the colliding snow particles, a separate set of sampling was carried out. Two plastic capsule containers (6 cm diameter, 7 cm height) were used to collect falling snow particles at the experimental location. Before the sampling started, both capsule containers were cleaned and then dried at 60°C for 1 hour. Afterwards their individual weights were measured. For every snowfall event, two samples were taken for evaluating mass and size of the falling snowflakes. Both capsule containers were kept against a dark background and the lid of the capsule containers were then taken off to collect falling snow particles for one minute. A video camera with a frame rate of 120 frames per second was used to record the collection process throughout the whole period. Afterwards the capsule containers were sealed and kept at room temperature (18°C) for a period of 2 hours to remove any precipitation on the outside of them, and then weighed afterwards. The resolution of the weighing scale was 0.001 milligrams.

4.4 Data Processing after Sampling

4.4.1 Workflow

The initial steps involved separating out required data from all the recorded videos and extracting individual frames, followed by processing of images (removal of distortion).
The recorded data in the form of video files were first inspected and time stamps for multiple sampling events were noted down. Each sampling event was then clipped from the original video and individual frames were extracted. The extracted images were then corrected for barrel distortion. Images of a checkboard (black and white boxes with known distance, as reference) were captured from both the cameras and camera parameters were extracted for both. The camera parameters were then applied to undistort the images. This step was done with the 'OpenCV' module in Python v3.7 (Bradski and Kaehler, 2008).

The measurements of the size of individual fragments were done manually using Image J software (Schneider et al, 2012). The calibration of the measuring scale in ImageJ was done in two steps. Firstly, the path of a random snowflake was identified, which did not collide with any of the ice spheres. The size of this snowflake was measured when it just reaches the same horizontal level as the array of ice spheres. This 1st measurement is not accurate as the size decreases with increasing distance from the camera lens. Afterwards, the size of the same snowflake was measured when it came in contact with the sugar solution tray, which had 2 cm wide grided lines drawn on it. Using the grid lines as a reference, the actual size of the snowflake was obtained from this 2nd measurement. Finally, the 1st measurement taken at the level of the ice spheres, was rescaled to match the actual measurement taken at the sugar solution tray. This calibration was maintained for measuring the sizes for incident snowflakes, ice spheres and the fragments.

A mean of five separate measurements, with the calibrated scale was considered to be final size while measuring each individual object (snowflake, ice sphere and fragments). Also, for each collision event, the fall speeds of the snowflakes were measured, by counting the number of frames and estimating the distance using ImageJ from their respective appearances in the image frames.

4.4.2 Extracting information from raw data

The processed images from the selected snowfall episode (24 February) were grouped as separate folders for each collision event. The grouped images were inspected, and the number of fragments was noted along with their measured sizes (after calibration), maintaining the workflow mentioned in Sec. 4.4.1 (the measured data for each collision event are shown in Table A1).

A similar workflow was followed for the mass-size sampling dataset as well. Clipping of required data from the original video files was followed by extraction of image frames, and removal of distortion. The snowflakes falling into both the capsule containers were counted and their sizes were measured using ImageJ software (same calibration). With information of the total mass and individual sizes of the snowflakes, the two unknown parameters (α, b) for the mass-size relation (Eq(1)) were calculated by solving two simultaneous equations.

Table 2. The raw data obtained from mass-size sampling from two capsule containers labelled Sample A and Sample B. The total mass (in kg) and the number of snowflakes counted for each of the two containers are shown.

	Sample A	**Sample B**
Total Mass (kg)	2.7×10^{-6}	1.6×10^{-6}
No of Snowflakes	91	74

Having obtained the mass-size parameters (α and b) from the observed data, this enabled the mass of each incident snowflake (for each collision event) to be estimated from measured size. That in turn enabled the CKE to be estimated (using Eq(3)) in conjunction with the measured fall speed.

4.5 Analysis of the Data from Field Observations

First, the fragment distribution and the uniformity of the observed data were checked before proceeding with further analysis. To characterise the observed data, plots indicating the relations between fall speed and particle size, between mass and size, and between CKE and fragments numbers, were generated (Sec. 5).

4.6 Application of the Fragmentation Scheme

An application of the field observations made in this project is to improve the accuracy of the theoretical formulation for fragmentation in ice-ice collisions. With the information on size, mass and CKE, the fragmentation scheme (Phillips et. al. 2017a; Sec. 3.6) was applied to each collision of snow in the chamber. This theoretical formulation predicted the number of fragments produced in each collision. Refitting of the formulation (obtaining the asperity-fragility coefficient C, from the observed data) was then performed so as to optimise agreement with observed data. The details of the refitting procedure are explained below.

4.6.1 Numerical approach for refitting the formulation

The masses of the snowflakes, sizes of snowflakes, sizes of ice spheres and estimated CKEs were fed as inputs into ice-ice breakup formulation (Sec. 3.6). From a list of observed and predicted numbers of fragments for all collision events in the chamber for the selected snowfall episode (24 February), the overall root mean square error and mean of the absolute magnitudes of the errors were calculated. In order to find the optimal values of the C, the fragmentation scheme was run over a range of C values, starting from its default value of 1.08×10^4 to almost 10^7. Finally, the value of C with minimum RMSE from all the iterations, was selected as the optimal value. The simulations for predicting the number of fragments from the theoretical formulation were done in Fortran programming language.

4.6.2 Estimation of cloud base and cloud top temperatures for observed case

The Hybrid Single-Particle Lagrangian Integrated Trajectory (HYSPLIT) model (Stein et al, 2015) has been used to verify the air trajectory during the sampling day (24th of February 2022). The HYSPLIT back trajectory (Figure 10 (a)) along with cloud radar data (WeatherOK Inc) has been used to locate the source of the air mass for the precipitating clouds for the sampling day, and further to get an approximate value of cloud base temperature as well. The precipitating cloud that produced the sampled snow was estimated to have formed earlier during advection in the vicinity of Ensjölkarna Nature Reserve, with coordinates 62°31′N, 15°53′E. The surface air temperature at this cloud formation location has been used to approximate the cloud base temperature (4^{o}C). The cloud radar (Figure 10 (b)) confirmed that the precipitating clouds, observed at the sampling location, indeed originated about 4 hours prior to the onset of sampling episode, near the Ensjölkarna Nature Reserve area.

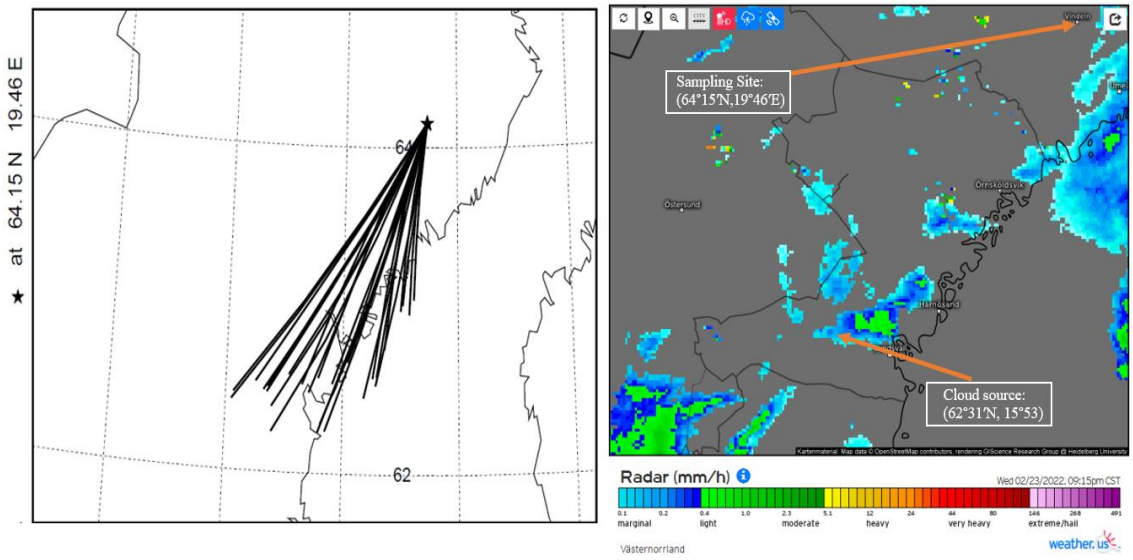

(a) HYSPLIT back trajectory, 4 hours prior to sampling, [adopted from NOAA] (b) Cloud radar, 4 hours prior to sampling, [adopted from WeatherOK Inc]

Figure 10. (a)Back trajectory analysis using HYSPLIT model for sampling location and (b) cloud radar data indicating the location with origination of precipitating clouds during the sampling episode on 24 February 2022. The back trajectory analysis was done for 4 hours prior to the start of sampling event, and so is the cloud radar image from the same time. The scale in the images are not the same.

[Sources: (a):https://www.ready.noaa.gov/HYSPLIT.php and (b):https://weather.us/radar-hd/vaesternorrland/20220224-0315z.html]

The cloud top temperature was estimated with the help of atmospheric sounding (vertical distribution of physical properties such as temperature, pressure, wind speed, wind direction, liquid water content etc in the atmosphere) dataset obtained from the European Centre for Medium-Range Weather Forecasts (ECMWF) ERA5 reanalysis data. The cloud top temperature was derived from this dataset by analysing the relative humidity profile. In the vertical direction, the level where the relative humidity drops below 100% is considered as the approximate mixed-phase cloud top. It was found to be -20^{o}C.

4.6.3 Estimation of rime fraction of sampled snow

In order to apply the formulation to the sampled snow fragmentation, it was necessary to provide it with the rime fraction of each snow particle as an input. This fraction was estimated as follows.

Since the observed case on 24 February has not been simulated directly, an alternative similar case of orographic clouds was instead. This alternative case involved observations during the ARM (Atmospheric Radiation Measurement) Cloud-Aerosol-Precipitation Experiment (ACAPEX) campaign on 7 February 2015, near California, and has been simulated with the Aerosol-Cloud (AC) model (Phillips et al, 2008, 2013, 2017b). This case had a cloud base at about 5^{o}C and mixed-phase cloud top at about -22^{o}C. These cloud base and cloud top temperatures resemble those observed over the present study location (24 February) in Sweden. Here, the rime fraction, χ , is defined as the fraction of the total snow mass that is rime (cloud droplets frozen on impact). Typical values of the rime fraction of snow were

predicted by AC model for the ACAPEX simulation, in the range of about 0.16, averaged over all sizes and over the depth of similar cloudy columns.

From the observation data (24 February) the snow particle concentration near the ground was measured as 12 m^{-3} and the snow mass content was observed to be 6.59×10^{-3} kg m^{-3} at the sampling location in Sweden. For estimating the χ values at each snow particle size, the rime mass content of snow for all sizes was inferred by multiplying the estimated fraction of 0.16 by the observed snow mass content (6.59×10^{-3} kg m^{-3}). A look up table to yield the dependency of χ for each particle on its size (D) was constructed by applying these values of snow concentration, snow mass content and snow rime mass content to the AC bin microphysics scheme for a single grid point. An initial guess of $\chi(\mathrm{D})$ was set to 0 below 300 µm and to unity above 2 mm, being linearly interpolated over size in between. Then $\chi(\mathrm{D})$ was rescaled so as to match the total rime mass content of snow, summed over all the bins, with that inferred.

This yielded the estimated function, $\chi(\mathrm{D})$, for any snow particle size for the observed case (24 February). With this assumed *'uniform ramp'* form of the size dependency of χ (Figure 11), the fragmentation formulation (Sec. 3.6) was then re-fitted using $\chi(\mathrm{D})$ the size varying interpolated χ values, which gave us an optimized C.

The evidence underpinning this new 'uniform ramp' form of $\chi(\mathrm{D})$ is that the axial ratio of snowflakes sampled for collisions in the chamber was observed to be approximately constant in the range of 0.2 to 0.4 for all sizes (about 1 to 13 mm), (Sec. 5.3). Generally, any riming of snow naturally tends to restore the axial ratio towards unity, as snow transitions towards becoming graupel.

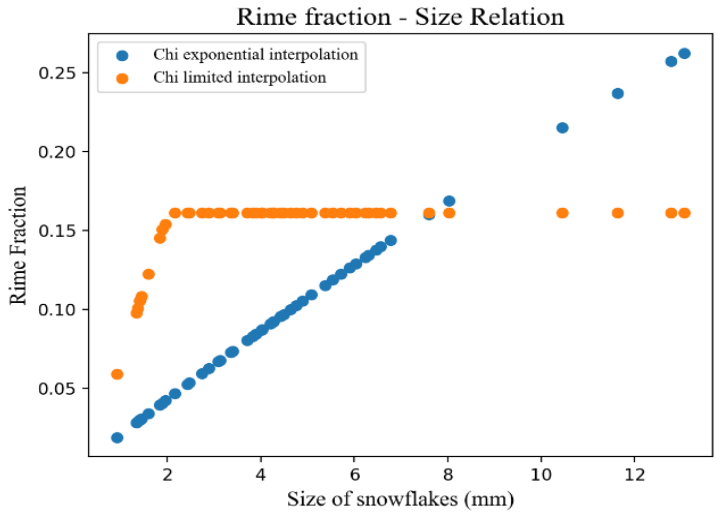

Figure 11: The exponential approach used in the original formulation (in blue) and subsequent estimation (in orange) for size dependent rime fraction [$\chi(\mathrm{D})$] is shown in figure 11. The assumed 'uniform ramp' form of rime fraction on size of the incident snowflake can be clearly seen in the figure (orange).

5. Results

5.1 Fragments Size Distribution

The fragment size distribution for the entire dataset of all collisions (49) is plotted (Figure 12) from estimates of numbers of fragments in each the 6 bins (Table A2). Here N denotes the number of fragments in each bin and D (mm) is the snowflake maximum dimension. Total number of fragments from all the 49 collision events were found to be 720.

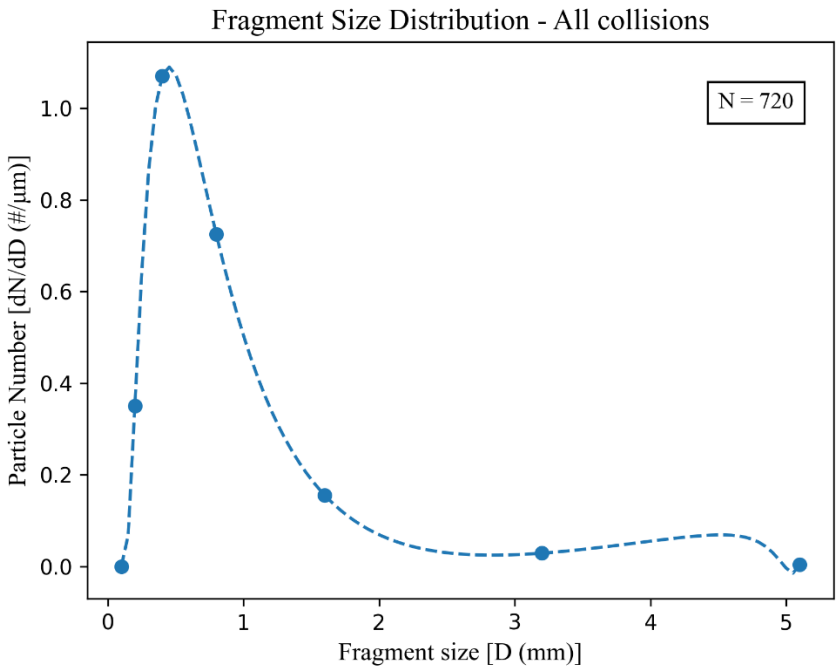

Figure 12: Fragment size distribution plot for the observed fragments from all sampled collisions (49). dN is the number of fragments in each bin, and D (mm) is the snowflake maximum dimensions. The plot is normalised in µm scale.

Figure 12 shows a peak at a fragment size of about 0.49 mm, which is about 10.8% of the mean incident snow particle size (4.6 mm) for all the collisions. The shape of the distribution curve is more nearly lognormal than normal, and there is a strong skewness with a tail towards the larger sizes of the parent particle when plotted as a function of size.

To illustrate the variability among different collisions, fragment size distributions for 3 randomly selected collisions with contrasting sizes (from the observed dataset) of the incident parent snowflakes are shown in Figure 13. The sizes of the snowflakes were: 1.4, 6.4 and 12.7 mm. Their corresponding number of fragments were 8, 24 and 28 respectively. The peaks of the fragment size distributions occur at fragment sizes of about 20% , 8% and 6% of the parent snow particle sizes respectively.

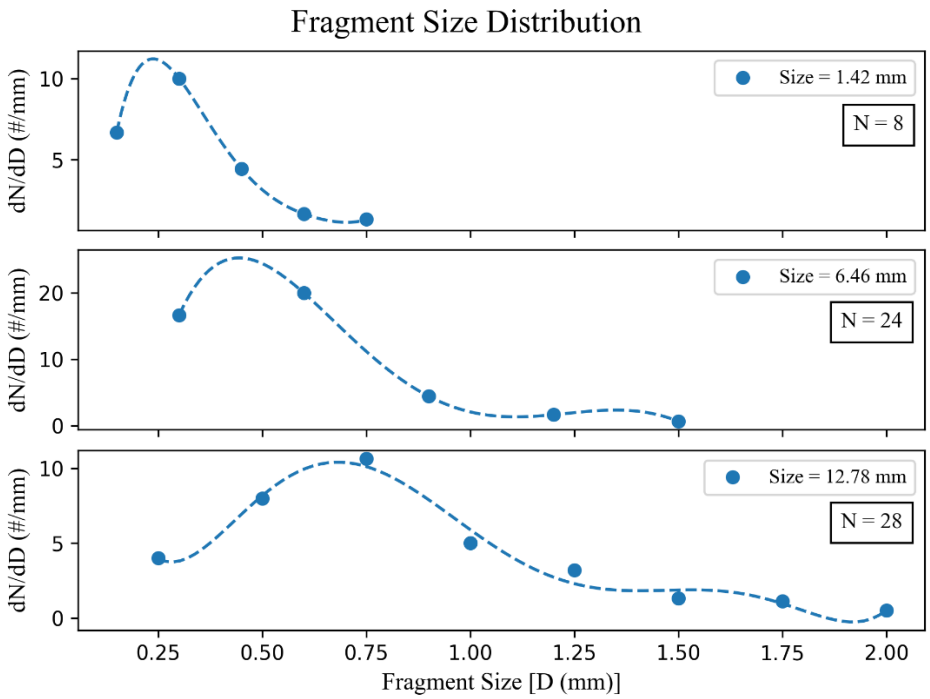

Figure 13: Fragment size distribution plot for 3 different sizes of the incident parent snow particles. dN is the number of fragments for each bin, and D (mm) is the snowflake maximum dimensions. The plots are normalised in mm scale.

5.2 Fall Speed and Size variation

The relation between fall speed (or terminal velocity) in cm/s and size of snowflakes in mm is shown in Figure 14. A curve fit line is also shown for the two variables.

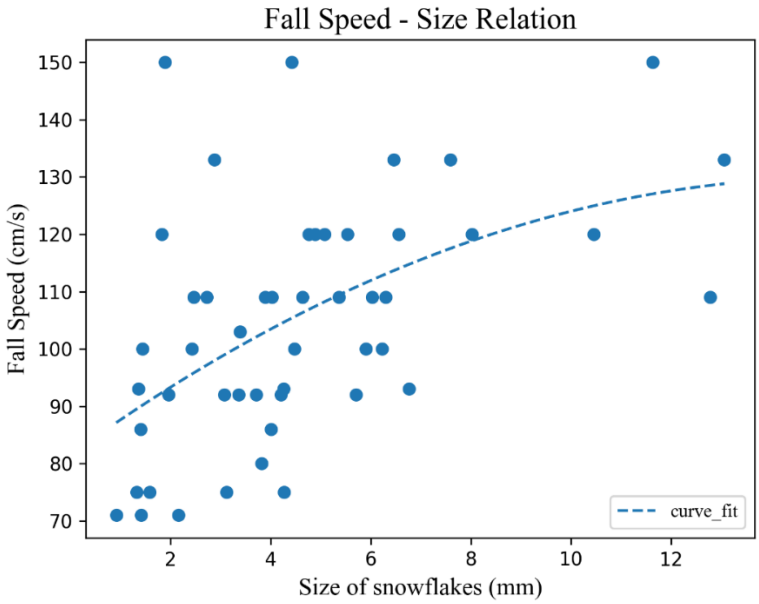

Figure 14: Fall speed (cm/s) and size of snowflakes (mm) are plotted against each other.

5.3 Mass-Size Relationship

A comparison table (Table 3) between experimentally derived mass-size parameters (α and b) and reported values of these parameters from the literature for the dendritic and needle shaped ice crystals is shown here. Units of mass are in grams and sizes are in cm.

Table 3: Comparison with previously reported values of α and b for different ice crystals, and values of α and b obtained from field observation conducted in this present study. Here mass is in gm and size in cm.

Crystal type	$\boldsymbol{\alpha}$ **(g/cm)**	**b**
Planar dendrite (Yau and Rogers, 1996, their Ch 9)	3.8×10^{-4}	2
Needle (Yau and Rogers, 1996, their Ch 9)	2.9×10^{-5}	1
Planar dendrite (Pruppacher and Klett 1997, their Ch 2)	6.1×10^{-4}	2.29
Needle (Pruppacher and Klett 1997, their Ch 2)	4.9×10^{-5}	1.8
Aggregates of unrimed dendrites (Locatelli and Hobbs, 1974)	7.3×10^{-5}	1.4
Aggregates of densely rimed dendrites (Locatelli and Hobbs, 1974)	3.7×10^{-5}	1.9
Observed in present study	$\mathbf{1.2 \times 10^{-4}}$	**0.87**

Figure 15 shows the plot of mass (mg) and size (mm) relationship for the experimentally observed data set during the sampling event.

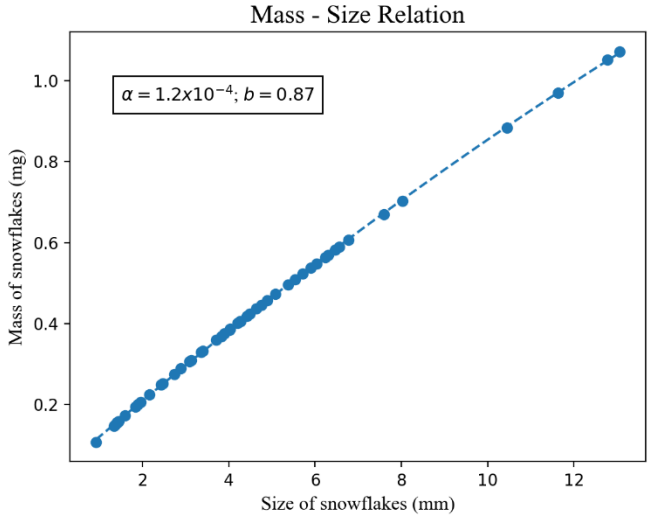

Figure 15: Relationship between mass (mg) and size (mm) plot for each incident snowflake is shown here.

The variation of axial ratio (width to length) and size of the incident snowflakes are shown in Figure 16. The average axial ratio was found to be 0.33 for the incident snowflakes undergoing fragmentation

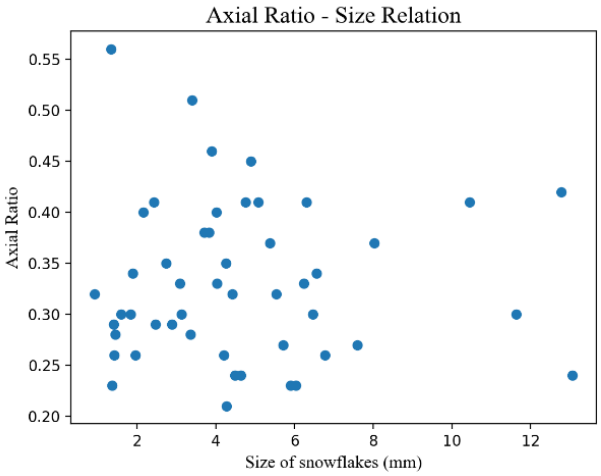

Figure 16: Variation of axial ratio with size of incident snowflakes inside the chamber.

5.4 Variation of the Number of Fragments with Sizes of the Colliding Particles

Here in Figure 17, the variation in number of fragments (on z-axis) observed and predicted for different sizes of snowflakes (x-axis) and ice spheres (y-axis) are shown in a 3D plot. The modelled number of fragments had size-dependent rime fraction values assuming the 'uniform ramp' form of $\chi(D)$, (Sec. 4.6.3) and the optimum value of $C = 3.86 \times 10^4 \text{J}^{-1}$. The correlation coefficient (r) between observed and predicted numbers of fragments was 0.71.

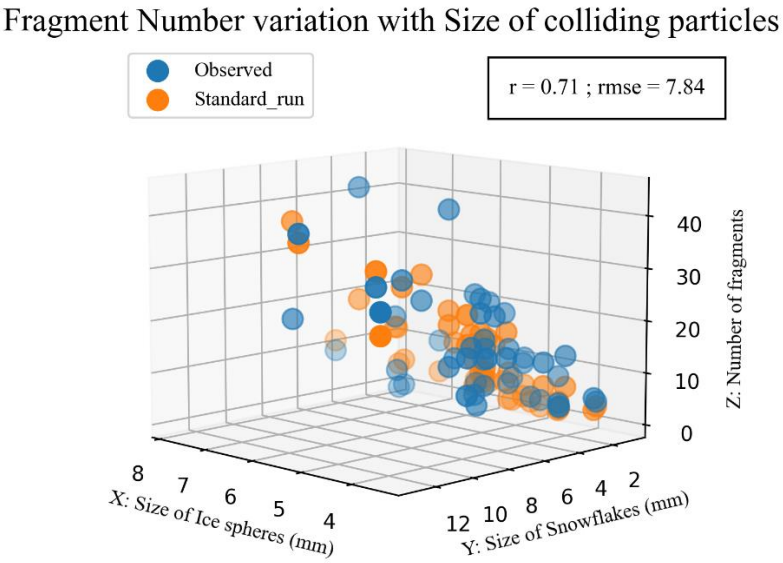

Figure 17: A 3D scatter plot showing number of fragments (z-axis) variation for different sizes of ice spheres (y-axis) and different size of snowflakes (x-axis) for each collision event.

5.5 Comparison between Observations and Predictions

Figure 18 shows a comparison of the number of fragments predicted with that observed. Four cases of predictions scenarios were compared for observed number of fragments.

Firstly, with unmodified default parameters ($\chi = 0.1$, $C = 1.08 \times 10^4$ J^{-1}) of the fragmentation scheme (labelled as 'Unmodified' in Figure18). Secondly, with a fixed χ value of 0.16 (labelled as 'Modified Constant X' in Figure18), with $C = 4.48 \times 10^4$ J^{-1}. Third, a modified version of the formulation with originally exponentially varying size dependent χ. Labelled as 'Modified Exponential X'. This gave a value of $C = 1.69 \times 10^4$ J^{-1}. And lastly the 'Modified Standard Run', another modified version of the formulation with 'uniform ramp' shaped size dependence on χ (Sec. 4.6.3), which gave a value of $C = 3.86 \times 10^4$ J^{-1}.

A positive skewness is also seen for all the cases: observed and 4 modified scenarios of the formulation scheme.

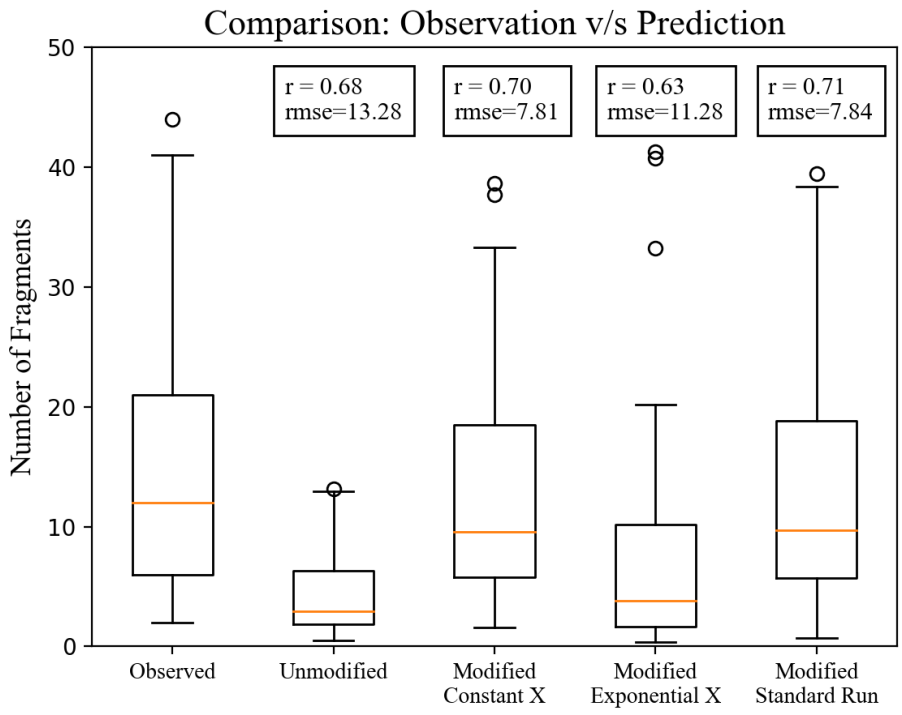

Figure 18: A comparison between number of fragments observed with that of predicted number from the fragmentation scheme for i) with default parameters (Unmodified), ii) fixed rime fraction of 0.16 (Modified Constant χ), iii) for originally exponential variation of size dependent rime fraction (Modified Exponential χ), and iv) for 'uniform ramp' shaped size dependency on the rime fraction (Modified Standard Run). The correlation coefficient (r) for each of the prediction scenarios with observed number of fragments in chronological order were 0.68, 0.70, 0.63 and 0.71, respectively; and their respective RMSE values were: 13,28, 7.81, 11.28 and 7.84.

A summary of the overall results is shown in Table 4. The correlation between observed and predicted number of fragments, along with their errors, and optimal values of ψ, χ and C for each of the predicted scenarios is also given here.

Table 4: A comparison of results from all the simulations done using the theoretical formulation for predicting the number of fragments. Their correlation with field observations, errors, optimal values for: sublimational correction factor ψ, rime fraction χ, and asperity fragility coefficient C (J^{-1}) is shown here

	Mean fragments	**Correlation with Observed data**	**RMSE**	**Mean absolute error**	$\boldsymbol{\psi}$	$\boldsymbol{\chi}$	$\boldsymbol{C}$ **(J^{-1})**
Unmodified Prediction (Phillips et al, 2017a, constant riming fraction)	4.19	0.68	13.28	10.23	3.5×10^{-3}	0.1	1.08×10^{4}
Modified Constant χ (constant riming fraction)	12.75	0.70	7.81	1.72	1.45×10^{-2}	0.16	4.48×10^{4}
Modified Exponential χ (original form of riming fraction)	8.26	0.63	11.28	6.2	5.5×10^{-3}	Exponential variation	1.69×10^{4}
Modified Standard Run (Standard run)	12.83	0.71	7.84	1.64	1.25×10^{-2}	'Uniform ramp' shape	$\mathbf{3.86 \times 10^{4}}$
*Mean number of fragments from observations = 14.47							

5.6 Variation of fragment number with CKE

The variation of number of fragments produced for both observed and modified standard run (uniform ramp) values with CKE (Joules) is shown in Figure 19. Also fitted lines are shown for the observed data, prediction (dotted) with standard run and prediction (solid) with default exponential increase of rime fraction (green) in Figure 19.

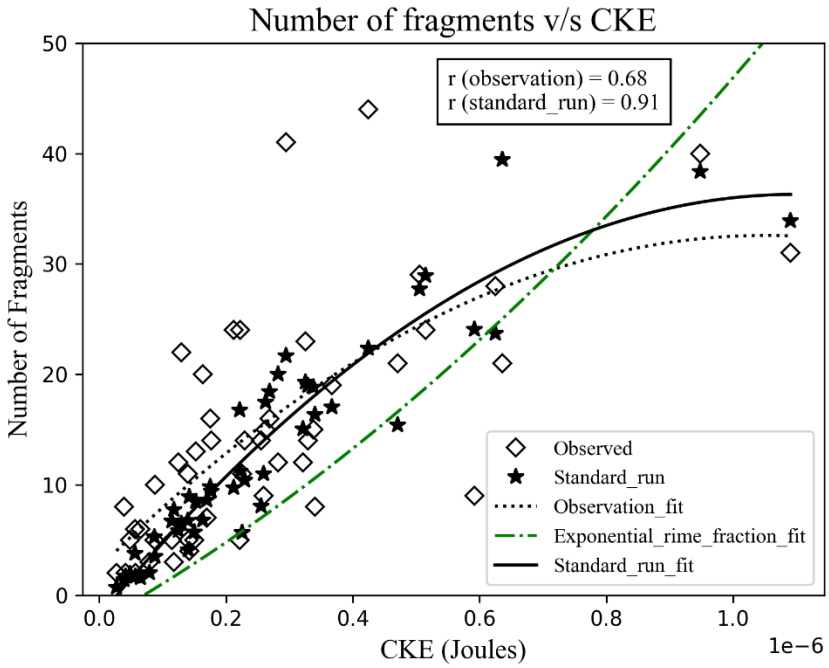

Figure 19: Variation of number of fragments per collision with CKE (Joules). Curve fitting is shown for observation (dotted), standard run (solid) and default exponential rime fraction variation (green) case.

6. Discussions

The initial inspection of the raw data showed that the process of fragmentation via collision of ice spheres and snowflakes has been captured effectively. As noted above only raw data from one of the 5 snowfall episodes has been analysed here (Sec. 4.3). Analysis of the data for other sampling days would be interesting to investigate as well and could be a part of future work.

The skewed bell shape of the fragment size distribution curve (Figure 12) is relatable to previously reported size distribution plots (Vardiman 1978a, his Figure 17). The peak of the distribution is typically at 0.4-0.6 mm which is much larger than the smallest detectable size of 0.15 mm. The shape also confirms that most of the fragments emitted were large enough to be detected. However, due to limited resolution of the video imagery there could also be a possibility of a hidden population of unseen fragments smaller than 0.15 mm that might have predominated in reality.

The fall speed and size variation plots were generated to validate the observations with previous studies. Yau and Rogers (1996, their Ch 9) reported similar observations for fall speed vs size of snowflakes for different crystal types. The observed data (Figure 14) corresponds to their relations for needle shaped ice crystals and mixed-habit crystals with droplets. Moreover, the curve fit shown in Figure 14 resembles the fall speed relationship for aggregates (Pruppacher and Klett 1997, their Ch 2). Locatelli and Hobbs (1974) also reported similar relationships between fall speed and size for various crystal types. The images shown in Figure 9 also confirm the dendritic regime of the snow particles seen during the selected snowfall episode (24 February).

The comparison shown in Table 3 of the mass-size relation parameters α and b, for the observed case and previously reported studies shows that the α parameters fall in between dendritic and needle shaped type of ice crystals (Locatelli and Hobbs, 1974; Yau and Rogers, 1996, their Ch 9; Pruppacher and Klett 1997, their Ch 2). However, parameter b is found to be slightly lower than in these observations from the literature. During mass-size sampling, all types of crystal were collected into the container capsules. Manual selection of a specific type of ice crystal during a snowfall event with mixed ice crystal types was not an easily achievable task. Another factor could be the error in counting and sizing the ice particles as they fell into the capsules from the imagery. The mass-size plot shown in Figure 15 does represent similar trajectory as reported for aggregates of rimed dendrites and aggregates of unrimed planar bullet shaped crystals (Locatelli and Hobbs, 1974; Pruppacher and Klett 1997, their Ch 2).

The observed number of fragments seemed to increase with the size of the colliding snow particles, with more fragments seen for larger sizes. This was partly due to increasing CKE and partly from increasing contact area (Dash et al, 2001, Phillips et al, 2017a). These dependencies were adequately predicted by the formulation and a correlation coefficient of 0.71 was seen between the observation and the modified standard run (‘uniform ramp’

variation of rime fraction, Figure 11) of the formulation. However, the number of fragments produced is dependent on other factors, some of which are uncertain such as the fraction of riming of the particles and the exact mass of each incident snowflake. It was found during the simulations with the formulation that the predicted number of fragments was highly sensitive to rime fraction (doubling the rime fraction can more than double the predicted fragment number). This justifies the approach used for estimating the rime fraction as a function of size (Sec. 4.6.3).

In the observed cases it was also seen that, often a bigger snowflake was found to produce a smaller number of fragments (but larger dimensions) when the angle of collision was not normal to the horizontal plane of the static ice spheres inside the chamber. This would often happen because the snow would retain some of its horizontal momentum when falling from the windy environment into the still air of the chamber. However, the angle of collisions was not measured in this study as in practice this is unlikely to be an issue because such oblique collisions happen anyway in real clouds and other issues of unrepresentativeness would seem more important. For example, the free fall of a natural graupel particle in a real cloud will change the numbers of fragments that remain stuck to its surface relative to a fixed ice sphere. Similarly, the surface of a natural graupel particle will be roughened by its coating of rime (Field et al, 2016), perhaps promoting fragmentation relative to our experiment.

Regarding the simulations of our observation with the formulation for various scenarios of rimed fraction, the 'Unmodified' version (with default values of the fragmentation scheme [χ = 0.1, $C = 1.08 \times 10^4$ J^{-1}]) underpredicted the number of fragments by approximately 3.5 times. Out of the scenarios the best agreement was for the 'Modified Standard Run' with a higher value of $C = 3.86 \times 10^4$ J^{-1} and constancy of the rime fraction over most snow sizes (Figure 18). This improves the model agreement compared to the original formulation (Phillips, et al, 2017a), for this study.

Further improvement can be done with better estimate of χ values for each incident snowflakes. A detailed case study and a simulation reproducing similar cloud system as observed during the sampling day would provide us with better estimates of rimed fraction for various types of ice particles observed during that day. With this information the fragmentation scheme designed by Phillips et al, (2017 a, b), could be further optimised. This is a part of the future work as a continuation to this study.

As stated before, the formulation of fragmentation scheme used in this study is based on conservation of energy (Phillips et al, 2017a). The initial kinetic energy before collision could be transferred into final kinetic energy after collision, change in surface adhesion energy as well as energy loss as heat, noise inelastic deformation (Phillips et al, 2017a). The correlation of CKE with the observed fragment number (r = 0.68) is slightly less than with predicted number (r = 0.91). However, the refitted formulation in Figure 19 follows a similar trajectory for both prediction and observations. The lower correlation seen in the observed case could be due to the variability among collisions of the impact angle and fragility and bulk density of the incident snow particles causing them to deviate from the inferred mass size relations.

6.1 Field Work

Ideally, the duration of data collection could have been longer to have a wider range of samples of snow from a variety of weather systems. An ideal situation would be to collect data over entire winter season. Indeed, a factor to consider is the type of snowfall: dry powder snow and smaller snowflakes tend to have weaker fragmentation as they were found to get attached to ice spheres instead of undergoing fragmentation upon collision. A light intensity snowfall with snow aggregates, as in the selected snowfall episode here, was the most favourable condition for studying fragmentation. But it occurred only once or twice during the entire field campaign of 3 weeks.

The presence of foggy conditions was sought so as to replicate a real in-cloud conditions. Sublimational weakening occurs outside clouds as snow falls through the ice-subsaturated environment (Bacon et al, 1998). An advantage of sampling within a forest canopy was indeed helpful as forest stands can hold the fog for longer time as compared to an open area. An improvement in this regard could be done in terms selection of sampling location. Opting for a site with higher altitude would help us reach more foggy conditions. Also, for such locations the probability of sampling different types of ice particles would be increased manifold due to higher frequency of precipitation event.

Regarding the design of the portable chamber, an upgrade would produce better results. Both temperature and relative humidity inside the chamber were initially found to be higher and lower than the ambient conditions respectively. This led to the need for a longer stabilization period prior to each sampling episode. Additional vents were designed during the data collection process to obtain better circulation of air. Later, frozen icepacks were used to lower the temperature inside the chamber as well as to provide a colder environment during the collision events in an attempt to reach conditions similar to mixed phase cloud conditions. Heat release from electronic components and light sources was also observed to a small extent after prolonged usage (more than 2 hours) and they indeed slightly warmed the interior of the chamber. Similar issues were also faced during Vardiman's (1978 a, b) experiment, but our use of modern LED lights helped in minimising this issue to some extent. Addition of air vents and icepacks, and keeping the light sources outside the chamber, were helpful. For sampling episodes with air temperatures lower than -5°C, warming from light sources was found to be negligible. In future, lights could also be set up in a ventilated layer around the chamber with cold air to completely avoid this issue.

An improvement to this design could be use of different material for the constructing the chamber. A material with higher thermal conductivity and higher porosity would be helpful. Use of a humidifier would be beneficial, which should be taken into consideration for future sampling. One could also make use of cameras with much higher frame rate and with higher resolutions. Such camera setups are usually bulky in nature and expensive and a trade-off would have to made while selecting one. Fragmentation events for different types of ice crystals under different environmental conditions (temperature and humidity) could help establish more concrete relation with the CKE for various types of collisions and colliding

particles. Use of dedicated Artificial Intelligence (AI) based deep learning techniques (such as high-resolution object tracking for sub micrometre particles) in processing of raw data captured during field experiments would be helpful in minimising human error to some extent. Another alternative improvement could be replacement of camera setup with laser or radar-based detection. However, all of these would require considerate amount of funding.

6.2 Sources of Error

Finally, there are several sources of errors in the measurements. One possibility could be position of the camera and the light sources in the chamber setup. The optics were thoroughly checked numerous times before taking field measurements, but an ideal situation would be position cameras on all the four faces, the top and the bottom of the chamber, to avoid extremely small fragments that could have been missed due to too few cameras and their limited resolution. In this case there is indeed a possibility that tinier fragments might have been missed.

Distortion correction of the extracted images was done carefully using camera calibration parameters. Yet, it could result in incorrect measurements. Even after correcting for distortion, there is still a chance of slight errors, as the measurement from the raw data is done manually.

As a rough estimation, an error of about 10% in counting and sizing the observed fragments is expected. The estimation is based on error in distortion correction, error in counting of the number of fragments and subsequent size measurements (esp. for measurements smaller than the minimum camera resolution of 0.2 mm). CKE estimated by Eq (3) has measurements of 2 entities (1^{st} order for mass m, and 2^{nd} order for squared velocity $\vec{v}^2$ term). Resulting in 3 times the possibility for error in CKE estimation. The prediction from the refitted formulation in the Standard Run deviates from the observed fragment number for any given collision by $\pm$30% (Figure 19).

7. Conclusion

This study shows that the SIP process via ice-ice collisions have been characterised quite effectively from the results presented in this report. Mass-size relationships and subsequent CKE variation seen in the observations correspond to previously reported studies from the literature. The conclusions are as follows:

1. For snow aggregates from the dendritic regime with maximum dimensions between 1 mm and 13 mm, impacting pure ice spheres of 3 mm to 8 mm in diameter, the number of fragments per collision was observed to be between 2 and 44 with an average of about 15 fragments per collisions. These observations were for one selected snowfall episode in Northern Sweden, during winter.
2. The size distribution of fragments in any collision was seen to have a single broad peak at around half a millimetre, with a long tail towards the larger sizes, even bigger than 1 mm. The modal size of fragments from all collisions was about 10% of the mean size of the parent snow particles. For individual collisions this fraction ranged from about 5% (largest parent snow particle) to 20 % (smallest parent snow particle).
3. Simulation of the observed collisions with a previously published formulation, Phillips et al. (2017a) (Sec. 3.6) revealed an underprediction of the number of fragments per collision by a factor of about 3 to 4 times. The refitting of the formulation created a good match to the observed data by using a value of $C = 3.86 \times 10^4$ J^{-1} for the asperity-fragility coefficient and by replacing the original exponential form of the size dependence of the rime fraction of snow by a new uniform-ramp form (χ=0 as sizes below 0.3 mm and 1 above 2 mm being linearly interpolated in between).

The over-arching aims (Sec. 2) of the study have been achieved, namely to characterise fragmentation in graupel-snow collisions for a representative snowfall event consisting of dendritic aggregates and to improve its representation for cloud models. Naturally more observations of a greater variety of snow morphologies are needed. In particular the riming fraction as seen by Vardiman (1978b) is a sensitive parameter affecting fragment numbers. Yet the methodology pioneered in the present study provides an opportunity for widening the observational basis of formulations for SIP via fragmentation due to collisions.

The specific research questions (Sec. 2) have been answered as follows. Firstly, it is demonstrated here that the graupel-snow collision fragmentation process can be experimentally observed by avoiding the difficulties of creating snow particles in the lab with an approach of sampling natural snow particles outdoors during precipitation events. Although the graupel-snow impact speeds in real clouds aloft can be much higher than the impact speeds in our chamber with fixed ice spheres (snow fall speeds were about 1m/s, while real graupel can fall much faster than that), the formulation by Phillips et al. (2017b) is based on the irrefutable law of conservation of energy and other concepts of classical mechanics, proving that the number of fragments is dependent dynamically on CKE rather than on impact speed per se. Since the observed dependency of number of fragments on CKE and surface area of the colliding particles is expected to be universal, then it is not necessary to observe

the graupel-snow collisions exactly as they would occur in a real cloud (Phillips et al, 2021). Secondly, it is shown here that the mass-size relationship can be observed in a simple way by collecting a few numbers of snowflakes inside a container and weighing the snowflakes collectively. Thirdly, the fragmentation was shown to conform with the theoretically expected dependencies on size (Figure 15) and CKE (Figure 19).

To conclude, our field observations imply that fragmentation in graupel-snow collisions is even more intense than had been depicted by the original version of the formulation. A new revised version of the formulation is proposed for use in cloud microphysics schemes of atmospheric models.

8. Future work

Future work would be to simulate a 3D deep convective cloud case (with conditions similar to the one observed in this study) and evaluate the changes in ice concentration number with the revised C values and compare it with ice concentration number observed from aircraft data recordings.

Along with that, a better estimation of rimed fraction is a necessity to further minimise the errors. A solution could be, using a parcel microphysics model to follow one crystal as it grows by vapour growth, riming and accretion (at a constant Temperature and Liquid Water Content). So as to obtain a better estimation of the rime fraction.

Processing and analysis of the data collected from other sampling episodes needs to be done, as information derived from more collision events would enable us to optimise the original formulation further. More sampling is required for different types of ice crystals, especially snow that is more heavily rimed. Also, we need to upgrade the existing chamber as discussed in Sec. 6.1

These steps would be helpful in supporting the results obtained from this study, which could be beneficial to the scientific community in developing more efficient cloud models.

References:

Atkins, P., Atkins, P. W., & de Paula, J. (2014). *Atkins' physical chemistry*. Oxford university press.

Bacon, N. J., Swanson, B. D., Baker, M. B., & Davis, E. J. (1998). Breakup of levitated frost particles. *Journal of Geophysical Research: Atmospheres*, *103*(D12), 13763-13775.

Bailey, M., & Hallett, J. (2004). Growth rates and habits of ice crystals between− 20 and− 70 C. *Journal of the Atmospheric Sciences*, *61*(5), 514-544.

Bradski, G., & Kaehler, A. (2008). *Learning OpenCV: Computer vision with the OpenCV library*. " O'Reilly Media, Inc.".

Dash, J. G., Mason, B. L., & Wettlaufer, J. S. (2001). Theory of charge and mass transfer in ice-ice collisions. *Journal of Geophysical Research: Atmospheres*, *106*(D17), 20395-20402.

Dong, Y., Oraltay, R. G., & Hallett, J. (1994). Ice particle generation during evaporation. *Atmospheric research*, *32*(1-4), 45-53.

Hallett, J., & Mossop, S. C. (1974). Production of secondary ice particles during the riming process. *Nature*, *249*(5452), 26-28.

Huang, S., Hu, W., Chen, J., Wu, Z., Zhang, D., & Fu, P. (2021). Overview of biological ice nucleating particles in the atmosphere. *Environment International*, *146*, 106197.

James, R. L., Phillips, V. T., & Connolly, P. J. (2021). Secondary ice production during the break-up of freezing water drops on impact with ice particles. *Atmospheric Chemistry and Physics*, *21*(24), 18519-18530.

Field, P. R., Lawson, R. P., Brown, P. R., Lloyd, G., Westbrook, C., Moisseev, D., ... & Sullivan, S. (2017). Secondary ice production: Current state of the science and recommendations for the future. *Meteorological Monographs*, *58*, 7-1.

Kanji, Z. A., Ladino, L. A., Wex, H., Boose, Y., Burkert-Kohn, M., Cziczo, D. J., & Krämer, M. (2017). Overview of ice nucleating particles. *Meteorological Monographs*, *58*, 1-1.

Locatelli, J. D., & Hobbs, P. V. (1974). Fall speeds and masses of solid precipitation particles. *Journal of Geophysical Research*, *79*(15), 2185-2197.

Lau, K. M., & Wu, H. T. (2003). Warm rain processes over tropical oceans and climate implications. *Geophysical Research Letters*, *30*(24).

Magono, C., & Lee, C. W. (1966). Meteorological classification of natural snow crystals. *Journal of the Faculty of Science, Hokkaido University. Series 7, Geophysics*, *2*(4), 321-335.

Murray, B. J., O'sullivan, D., Atkinson, J. D., & Webb, M. E. (2012). Ice nucleation by particles immersed in supercooled cloud droplets. *Chemical Society Reviews*, *41*(19), 6519-6554.

Phillips, V. T., DeMott, P. J., & Andronache, C. (2008). An empirical parameterization of heterogeneous ice nucleation for multiple chemical species of aerosol. *Journal of the atmospheric sciences*, *65*(9), 2757-2783.

Phillips, V. T., Demott, P. J., Andronache, C., Pratt, K. A., Prather, K. A., Subramanian, R., & Twohy, C. (2013). Improvements to an empirical parameterization of heterogeneous ice nucleation and its comparison with observations. *Journal of the Atmospheric Sciences*, *70*(2), 378-409.

Phillips, V. T., Yano, J. I., & Khain, A. (2017a). Ice multiplication by breakup in ice–ice collisions. Part I: Theoretical formulation. *Journal of the Atmospheric Sciences*, *74*(6), 1705-1719.

Phillips, V. T., Yano, J. I., Formenton, M., Ilotoviz, E., Kanawade, V., Kudzotsa, I., ... & Tessendorf, S. A. (2017b). Ice multiplication by breakup in ice–ice collisions. Part II: Numerical simulations. *Journal of the Atmospheric Sciences*, *74*(9), 2789-2811.

Phillips, V. T., Yano, J. I., Deshmukh, A., & Waman, D. (2021). Comment on “Review of experimental studies of secondary ice production” by Korolev and Leisner (2020). *Atmospheric Chemistry and Physics*, *21*(15), 11941-11953.

Pruppacher, H. R., & Klett, J. D. (1997). Microphysics of Clouds and Precipitation, Springer Publications.

Radar HD from 02/23/2022, 09:15pm - Sweden. (n.d.). Retrieved from Weather.us https://weather.us/radar-hd/sweden/20220223-2150z.html

Schneider, C. A., Rasband, W. S., & Eliceiri, K. W. (2012). NIH Image to ImageJ: 25 years of image analysis. *Nature methods*, *9*(7), 671-675.

Sotiropoulou, G., Ickes, L., Nenes, A., & Ekman, A. M. (2021). Ice multiplication from ice–ice collisions in the high Arctic: sensitivity to ice habit, rimed fraction, ice

type and uncertainties in the numerical description of the process. *Atmospheric Chemistry and Physics*, *21*(12), 9741-9760.

Stein, A. F., Draxler, R. R., Rolph, G. D., Stunder, B. J., Cohen, M. D., & Ngan, F. (2015). NOAA's HYSPLIT atmospheric transport and dispersion modeling system. *Bulletin of the American Meteorological Society*, *96*(12), 2059-2077.

Takahashi, T., Nagao, Y., & Kushiyama, Y. (1995). Possible high ice particle production during graupel–graupel collisions. *Journal of the atmospheric sciences*, *52*(24), 4523-4527.

Vardiman, L. (1978a). *The Generation of Secondary Ice Particles in Clouds by Crystal–Crystal Collision*. [PhD Thesis. Colorado, USA: Colorado State University]

Vardiman, L. (1978b). The generation of secondary ice particles in clouds by crystal–crystal collision. *Journal of Atmospheric Sciences*, *35*(11), 2168-2180.

Yano, J. I., & Phillips, V. T. J. (2011). Ice–ice collisions: An ice multiplication process in atmospheric clouds. *Journal of the Atmospheric Sciences*, *68*(2), 322-333.

Yau, M. K., & Rogers, R. R. (1996). *A short course in cloud physics*. Elsevier.

Zhao, X., & Liu, X. (2021). Global Importance of Secondary Ice Production. *Geophysical Research Letters*, *48*(11), e2021GL092581.

Zhao, X., Liu, X., Phillips, V. T., & Patade, S. (2021). Impacts of secondary ice production on Arctic mixed-phase clouds based on ARM observations and CAM6 single-column model simulations. *Atmospheric Chemistry and Physics*, *21*(7), 5685-5703.

APPENDIX

A1. Data extracted from the Collision Events

The raw data from all the collision events were obtained after inspecting the video recordings and following the workflow mentioned in Sec. 4.4.1 Extracting images from the video recordings, distortion correction, calibration of measurement scale enabled us to measure the sizes (of the fragments, incident snowflakes and ice spheres), fall speeds of incident snowflakes, mass and estimation of CKE. A summary of these measurements and estimations are shown in Table A1

Table A1. The number of fragments, fall speed (in m/s) of incident snowflakes, sizes (in mm) of colliding snowflakes and ice spheres, their masses (in kg) and respective CKEs (in Joules) for all the 49 the collisions are shown.

Collision event	**Observed Fragments**	**Fall speed**	**Size of Snowflakes**	**Size of Ice Spheres**	**Mass of snowflakes**	**CKE**
		(m/s)	(mm)	(mm)	(kg)	(Joules)
1	3	0.8	3.82	6.78	3.69E-07	1.18E-07
2	9	1.09	4.64	7.84	4.37E-07	2.59E-07
3	44	1.2	6.56	6.61	5.90E-07	4.25E-07
4	5	0.75	1.59	5.29	1.72E-07	4.85E-08
5	22	0.92	3.08	5.18	3.06E-07	1.30E-07
6	5	1.09	2.47	5.65	2.53E-07	1.50E-07
7	24	1	4.48	4.87	4.24E-07	2.12E-07
8	12	1.2	4.76	5.29	4.47E-07	3.21E-07
9	11	0.92	3.36	5.19	3.30E-07	1.40E-07
10	5	1.2	1.83	3.48	1.95E-07	1.40E-07
11	6	0.93	1.36	5.29	1.51E-07	6.51E-08
12	5	0.75	3.12	3.79	3.09E-07	8.70E-08
13	8	0.71	1.42	4.35	1.56E-07	3.94E-08
14	5	0.75	4.27	5.06	4.06E-07	1.14E-07
15	10	0.92	1.96	4.87	2.07E-07	8.75E-08
16	28	1.09	12.78	3.87	1.05E-06	6.25E-07
17	5	0.92	5.71	4.52	5.23E-07	2.21E-07
18	2	0.71	0.92	4.87	1.07E-07	2.70E-08
19	12	1	2.43	6.42	2.49E-07	1.25E-07
20	4	0.86	4.01	6.6	3.85E-07	1.42E-07
21	2	0.86	1.41	4.34	1.55E-07	5.74E-08
22	16	0.93	4.26	4.87	4.06E-07	1.75E-07
23	15	0.93	6.77	4.34	6.06E-07	2.62E-07
24	3	1	1.44	4.89	1.58E-07	7.91E-08
25	9	1.33	7.59	4.06	6.69E-07	5.92E-07
26	2	0.75	1.33	4.36	1.48E-07	4.15E-08
27	6	0.71	2.16	3.42	2.25E-07	5.67E-08
28	21	1.2	10.45	6.52	8.84E-07	6.36E-07
29	24	1.33	6.46	5.36	5.82E-07	5.15E-07
30	41	1.09	5.37	5.2	4.96E-07	2.95E-07

31	8	1.2	5.08	6.36	4.72E-07	3.40E-07
32	40	1.33	13.06	5.37	1.07E-06	9.48E-07
33	23	1.09	6.03	4.33	5.48E-07	3.26E-07
34	12	1	6.23	4.89	5.64E-07	2.82E-07
35	31	1.5	11.63	4.38	9.70E-07	1.09E-06
36	29	1.2	8.02	5.19	7.02E-07	5.06E-07
37	19	1.2	5.54	6.23	5.09E-07	3.67E-07
38	14	1.03	3.39	4.68	3.33E-07	1.76E-07
39	7	0.92	4.21	4.89	4.01E-07	1.70E-07
40	15	1.09	6.3	4.12	5.69E-07	3.38E-07
41	24	1.09	3.89	5.19	3.75E-07	2.23E-07
42	16	1	5.9	4.56	5.38E-07	2.69E-07
43	14	1.2	4.89	4.22	4.57E-07	3.29E-07
44	13	0.92	3.71	3.89	3.60E-07	1.52E-07
45	11	1.5	1.89	4.87	2.00E-07	2.25E-07
46	14	1.09	4.03	4.93	3.86E-07	2.30E-07
47	20	1.09	2.73	4.99	2.76E-07	1.64E-07
48	21	1.5	4.42	4.61	4.19E-07	4.71E-07
49	14	1.33	2.88	3.74	2.89E-07	2.55E-07

A2. Grouped Data for Fragment Size Distribution

To visualise the fragment size distribution from all the collisions, 6 size bins were created. The size of a subsequent bin is double than that of the previous bin. Starting with 100 µm for the 1st bin, the size of subsequent bin was of 200 µm, 400 µm, 800 µm, 1600 µm and 3200 µm. All the fragment sizes were measured and put into their respective bin. In total there were 720 fragments counted for all the 49 collision events. The fragment size distribution obtained from this dataset is shown in Figure 12 (Sec. 5.1).

Table A2. Showing the grouping of the different size bins (in µm), bin interval length (in µm), and the number of fragments in each bin.

Intervals (µm)	100-200	200-400	400-800	800-1600	1600-3200	3.200-6.400
Interval size (µm)	100	200	400	800	1600	3200
Fragment Number in each bin	35	214	290	124	46	11